Lattice distortion in the spin-orbital entangled state in RVO$_3$ perovskites

J.-Q. Yan [1,*], W. Tian,[2] H. B. Cao,[2] S. Chi,[2] F. Ye,[2] A. Llobet,[3] A. Puretzky,[4] Q. Chen,[5] J. Ma,[6] Y. Ren,[7] J.-G. Cheng,[8] J.-S. Zhou,[9] M. A. McGuire,[1] and R. J. McQueeney[10]

[1]*Materials Science and Technology Division, Oak Ridge National Laboratory, Oak Ridge, Tennessee 37831, USA*
[2]*Neutron Scattering Division, Oak Ridge National Laboratory, Oak Ridge, Tennessee 37831, USA*
[3]*P-23, Neutron Science and Technology, Los Alamos National Laboratory, Los Alamos, New Mexico 87545, USA*
[4]*Center for Nanophase Materials Sciences, Oak Ridge National Laboratory, Oak Ridge, Tennessee 37831, USA*
[5]*Department of Physics and Astronomy, University of Tennessee, Knoxville, Tennessee 37996, USA*
[6]*Key Laboratory of Artificial Structures and Quantum Control, School of Physics and Astronomy,*
Shanghai Jiao Tong University, Shanghai 200240, People's Republic of China
[7]*X-ray Science Division, Argonne National Laboratory, Argonne, Illinois 60439, USA*
[8]*Beijing National Laboratory for Condensed Matter Physics, and Institute of Physics, Chinese Academy of Sciences,*
Beijing 100190, People's Republic of China
[9]*Materials Science and Engineering Program, University of Texas at Austin, Austin, Texas 78712, USA*
[10]*Ames Laboratory and Department of Physics and Astronomy, Iowa State University, Ames, Iowa 50011, USA*

We report a thorough study of Y$_{0.7}$La$_{0.3}$VO$_3$ single crystals by measuring magnetic properties, specific heat, thermal conductivity, Raman scattering, x-ray and neutron diffraction with the motivation of revealing the lattice response to the spin-orbital entanglement in RVO$_3$. Upon cooling from room temperature, the orbitally disordered paramagnetic state changes around $T^* \sim 220$ K to a spin-orbital entangled state which is then followed by a transition at $T_N = 116$ K to C-type orbital-ordered (OO) and G-type antiferromagnetic ordered (AF) ground state. In the temperature interval $T_N < T < T^*$, the VO$_{6/2}$ octahedra have two comparable in-plane V-O bonds which are longer than the out-of-plane V-O1 bond. This octahedral site distortion supports the spin-orbital entanglement of partially filled and degenerate yz/zx orbitals. However, this distortion is incompatible with the steric octahedral site distortion intrinsic to orthorhombic perovskites. Their competition induces a second-order transition from the spin-orbital entangled state to a C-OO/G-AF ground state where the long-range OO suppresses the spin-orbital entanglement. Our analysis suggests that the spin-orbital entangled state and G-OO are comparable in energy and compete with each other. Rare-earth site disorder favors the spin-orbital entanglement rather than a cooperative Jahn-Teller distortion. The results also indicate for LaVO$_3$ a C-OO/G-AF state in $T_t \leqslant T \leqslant T_N$ and an orbital flipping transition at T_t.

I. INTRODUCTION

RVO$_3$ (R = rare earth and Y) perovskites, in which V^{3+} has an electronic configuration of t_{2g}^2, show a series of spin- and orbital-ordering states below room temperature and have been an ideal materials playground for the study of complex coupling between spin, orbital, and lattice degrees of freedom of t_{2g} electrons [1]. Despite the fact that the spin and orbital ordering patterns of RVO$_3$ perovskites can be well understood following Goodenough-Kanamori rules [2,3], the quantum effects are widely believed to be important for understanding the spin- and orbital-ordered ground states due to a weak Jahn-Teller coupling of t_{2g} electrons. It has been under hot debate whether the classical Jahn-Teller orbital physics, quantum orbital fluctuations, or a close interplay between them better account for the unusual behavior of t_{2g} electrons in vanadate perovskites [4–14]. In addition to the competition between different spin-/orbital-ordered ground states, spin-orbital entanglement from Kugel-Khomskii (KK)-type superexchange interactions [15] competes with the long-range ordered states and should be considered when understanding the orbital physics in RVO$_3$ perovskites [16].

Spin-orbital entanglement resulting from the relativistic intrasite spin-orbit coupling can induce, via interacting with electron correlations and crystal electric fields, various emergent quantum phases and transitions in heavy transition metal compounds [17]. For 3d transition metal ions with a small relativistic on-site spin-orbit coupling, KK-type superexchange interactions lead to spin-orbital entanglement when degenerate 3d orbitals are partially occupied and orbital and spin degrees of freedom should be treated on equal footing. With the largest rare-earth ions among RVO$_3$ members, the pseudocubic LaVO$_3$ has been extensively studied to understand the effect of orbital fluctuations on the magnetic ground state and anisotropic optical properties [6–9,18–20]. A detailed experimental study [21] on LaVO$_3$ single crystal suggests a spin-orbital entangled state in the temperature range $T_N = 143$ K $< T < T^* \approx 200$ K. Despite careful neutron- and synchrotron-diffraction studies [21–25], the octahedral
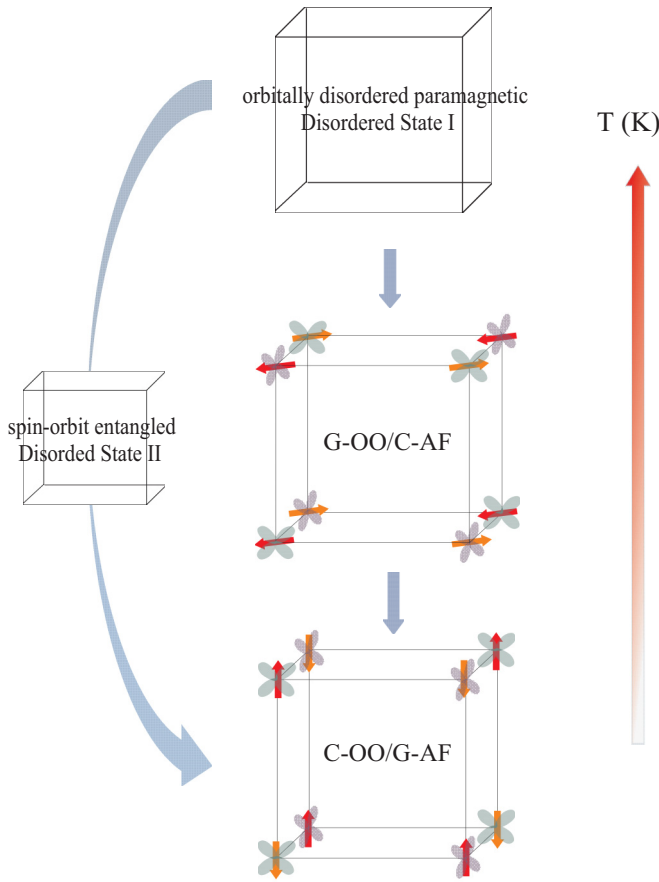
*yanj@ornl.gov

FIG. 1. Two different routes to the C-OO/G-AF state from the orbitally disordered paramagnetic state in RVO$_3$. OO—orbital ordering. AF—antiferromagnetic. Only yz and zx orbitals are plotted. xy orbital is occupied on every V site. yz and zx orbitals alternate in ab plane. G type: Out-of phase order along c axis. C type: In-phase arrangement along c axis. It should be noted that orbital order into G type occurs at a higher temperature than magnetic order into C type for R = Pr,...,Lu and Y.

distortion associated with the formation of the spin-orbital entangled state is unknown. The challenge comes from the fact that all three V-O bond lengths in LaVO$_3$ are comparable to each other above T_N. In LaVO$_3$, a first-order structural transition takes place at $T_t = 141$ K, just below $T_N = 143$ K [22,23]. The origin for this structural transition is unknown. As a consequence, the spin and orbital patterns in the narrow 2 K temperature window between T_N and T_t are under debate. It is worth mentioning that previous theoretical studies mainly investigate how the quantum fluctuations induce the G-type orbital-ordered (OO)/C-type antiferromagnetic (AF) ground state without considering the details and importance of possible spin and orbital ordering in that 2 K range.

A systematic study [26] on the spin and orbital ordering of Y$_{1-x}$La$_x$VO$_3$ shows that the spin-orbital entangled state (labeled as disordered state II in Ref. [26]) exists in a wide compositional range $0.2 < x \leqslant 1$. The comparative study between Y$_{1-x}$La$_x$VO$_3$ and RVO$_3$ suggests two different routes, as shown in Fig. 1, to the C-OO/G-AF state from the orbitally disordered paramagnetic state: either via the G-OO/C-AF state or the spin-orbital entangled disordered

state II. The former is observed in RVO$_3$ (R = Dy,...,Lu) and Y$_{1-x}$La$_x$VO$_3$ ($0 \leqslant x < 0.20$). Upon cooling from room temperature, these vanadate perovskites show a G-type orbital order around 200 K, a magnetic order around 100 K, and then an orbital flipping transition around 70 K to the C-OO/G-AF state. The latter route to the C-OO/G-AF state occurs in RVO$_3$ (R = Y and Tb) under high pressure [27], Y$_{1-x}$La$_x$VO$_3$ ($0.20 < x \leqslant 1.0$) [26], Y$_{1-x}$(La$_{0.234}$Lu$_{0.766}$)$_x$VO$_3$ [28], and Eu$_{1-x}$(La$_{0.254}$Y$_{0.746}$)$_x$VO$_3$ ($x > 0.9$) [29]. While the evolution with temperature of the nuclear structure in the former route has been extensively studied [4,30–35], a detailed investigation of the lattice response in the latter route is still absent [27,29].

In this paper, we present a thorough study of Y$_{0.7}$La$_{0.3}$VO$_3$ single crystals by a variety of techniques including magnetic measurements, specific heat, thermal conductivity, Raman scattering, x-ray and neutron diffraction. Compared to the pseudocubic LaVO$_3$ with three nearly identical V-O bonds, Y$_{0.7}$La$_{0.3}$VO$_3$ has a larger GdFeO$_3$-type distortion and has, at room temperature, one long, one medium, and one short V-O bond that could be well resolved with neutron powder-diffraction measurements. Therefore, Y$_{0.7}$La$_{0.3}$VO$_3$ provides an ideal material platform to study the local lattice change in the spin-orbital entangled state. Our structural study shows that the splitting between the in-plane V-O bonds becomes smaller upon cooling in the temperature range $T_N \leqslant T \leqslant$ 300 K. This provides strong evidence for the spin-orbital entanglement of degenerate yz and zx orbitals in the disordered state II. This structural response is incompatible with the octahedral site distortion intrinsic to orthorhombic perovskites and their competition induces a second-order transition from the spin-orbital entangled state to C-OO/G-AF ground state. Our analysis suggests that the spin-orbital entangled state and G-OO are comparable in energy and rare-earth-site disorder favors the spin-orbital entanglement rather than a cooperative Jahn-Teller distortion. The results also indicate for LaVO$_3$ a C-OO/G-AF state in the narrow range from $T_t \leqslant T \leqslant T_N$ followed by an orbital flipping transition at T_t.

II. EXPERIMENTAL DETAILS

Y$_{0.70}$La$_{0.30}$VO$_3$ single crystal was grown using an optical floating zone furnace in a procedure described elsewhere [11]. The room-temperature x-ray diffraction experiment on powder from pulverized single crystals confirmed the single phase and the diffraction pattern could be indexed in $Pbnm$ symmetry. A large thermoelectric power (>550 μV/K) at room temperature implies an essentially stoichiometric oxygen content. Elemental analysis confirmed the Y/La ratio of 7:3, which was carried out using a Hitachi-TM3000 microscope equipped with a Bruker Quantax 70 EDS system. The crystal quality was also confirmed by x-ray Laue diffraction. The single crystals were well oriented within an error of less than $1°$ for the study of anisotropic magnetic properties.

The magnetic properties were measured with a magnetic property measurement system (Quantum Design, QD) in the temperature interval 2 K $\leqslant T \leqslant$ 320 K. Specific heat was measured with a QD Physical Property Measurement System (PPMS) in the temperature interval 1.90 K $\leqslant x \leqslant$ 250 K. Thermal conductivity was measured from 1.9 K to 300 K

using the thermal transport option (TTO) from QD and a 14 T PPMS. A rectangular bar with the dimension of 0.70 mm × 0.75 mm × 8 mm was cut from a large crystal and used for the TTO measurement. Silver epoxy (H20E Epo-Tek) was utilized to provide mechanical and thermal contacts during the thermal transport measurements. Thermal conductivity measurement was performed along a random orientation because the heat transport in RVO$_3$ perovskites shows no directional dependence [11,28].

The Raman spectra were measured in a custom-built micro-Raman setup. The samples were excited with a continuous wave (cw) diode-pumped solid-state laser (Excelsior, Spectra Physics, 532 nm, 100 mW) through an upright microscope using a 50× long-working distance objective with NA (numeric aperture) = 0.5. The typical incident laser power on a sample was maintained at 100 μW to reduce possible laser heating and damaging of the samples during Raman spectra acquisition. The scattered Raman light was analyzed by a spectrometer (SpectraPro 2300i, Acton, f = 0.3 m) that was coupled to the microscope and equipped with an 1800 groves/mm grating and a CCD camera (Pixis 256BR, Princeton Instruments). The low-temperature Raman spectra were measured using a liquid He-cryostat (MicrostatHiRes-II, Oxford Instruments) with a temperature controller (MercuryiT, Oxford Instruments) that allowed precise temperature control from 3.6 to 300 K. The cryostat was mounted on a motorized XY microscope stage (Marzhauser) under the microscope of the micro-Raman setup. The cryostat was evacuated to the base pressure of 7×10^{-7} mbar prior to cool down.

The high-resolution x-ray single crystal diffraction was performed at 11ID-C, Advanced Photon Source, Argonne National Laboratory. Single crystal diffraction measurements were performed at 90 K < T_N, T_N < 130 K < T^*, and T^* < 300 K, respectively.

Part of the crystals were ground into fine powder for neutron powder diffraction measurements. Neutron powder diffraction was performed in the temperature range 12 K ⩽ T ⩽ 300 K at HIPD, Los Alamos Neutron Science Center, Los Alamos National Laboratory.

Single crystal neutron diffraction experiments were performed using HB-1A triple-axis spectrometer, HB-3A four-circle single crystal diffractometer, and the wide-angle neutron diffractometer (WAND) located at the High Flux Isotope Reactor (HFIR), and the elastic diffuse scattering spectrometer (Corelli) at Spallation Neutron Source (SNS) of the Oak Ridge National Laboratory. The HB-1A spectrometer operates with a fixed E_i = 14.6 meV employing a double pyrolitic graphite (PG) monochromator system. Two PG filters were mounted after each monochromator to significantly reduce higher order contaminations of the incident beam. The WAND diffractometer uses a vertically focused Ge (1 1 3) monochromator that provides a wavelength of 1.48 Å. The Y$_{0.7}$La$_{0.3}$VO$_3$ single crystal was oriented in [H 0 L] and [0 K L] scattering planes in the HB-1A and WAND experiments, respectively. For both experiments, the crystal was mounted on an aluminum plate, sealed with helium exchange gas, and cooled using a closed-cycle He refrigerator. Three patterns were collected at 4 K, 130 K, and 220 K using WAND by rotating the crystal with respect to the fixed position sensitive detector that covers 125 scattering angles.
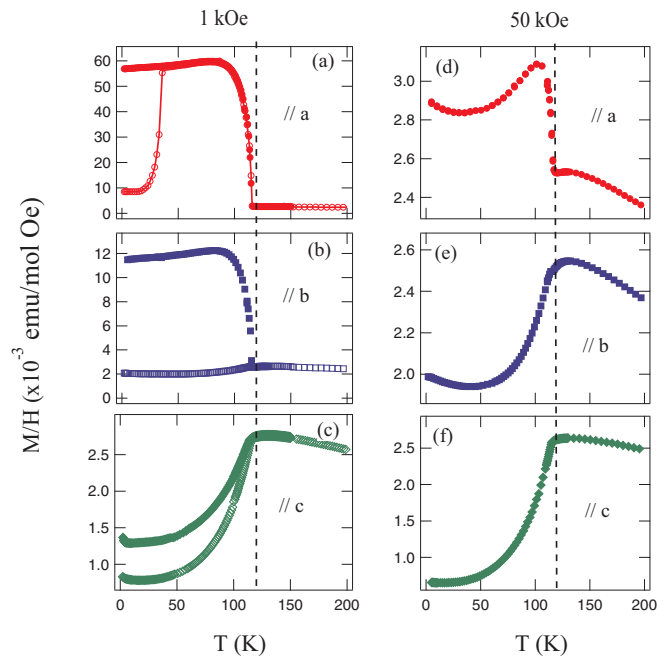

FIG. 2. Temperature dependence of magnetization measured in both zero-field-cooled (ZFC, open symbol) and field-cooled (FC, solid symbol) modes in an applied magnetic field of 1 kOe (a, b, c) and 50 kOe (d, e, f) along three different crystallographic axes of Y$_{0.7}$La$_{0.3}$VO$_3$. The anomaly around 40 K in ZFC curve in (a) comes from domain alignment.

Single-crystal neutron diffraction was performed to measure the nuclear structures at 5 K and 150 K and magnetic structure at 5 K, at the HB-3A four-circle diffractometer at HFIR. A neutron wavelength of 1.003 Å was used from a bent perfect Si-331 monochromator [36]. The neutron diffraction data refinements are based on 85 magnetic and nuclear reflections with the program FULLPROF.

III. RESULTS

A. Magnetization, specific heat, and thermal conductivity

The magnetization curves measured in zero-field-cooling (ZFC) mode are sensitive to a small remnant field of even only a few Oe. We thus quenched the magnet at 150 K before cooling to 2 K. Figure 2 shows the temperature dependence of the magnetization taken along three different crystallographic axes in the temperature range 2 K ⩽ T ⩽ 300 K and in an applied magnetic field of 1 kOe and 50 kOe, respectively. No anomalous diamagnetism, as in LaVO$_3$ [23,37,38], or magnetization reversal, as in YVO$_3$ [39–41], was observed in the whole temperature range. One magnetic transition at 116 K could be well resolved in all the curves measured with fields along different crystallographic directions. The temperature dependence of the magnetization suggests an AF order at T_N = 116 K. A weak canted-spin ferromagnetic component was observed along the a axis below T_N. The canted-spin ferromagnetic component along the b axis is much weaker and can be observed in a small magnetic field. This weak canted ferromagnetism might be from the misalignment of crystals during measurement, which picks up a small contribution from a axis.
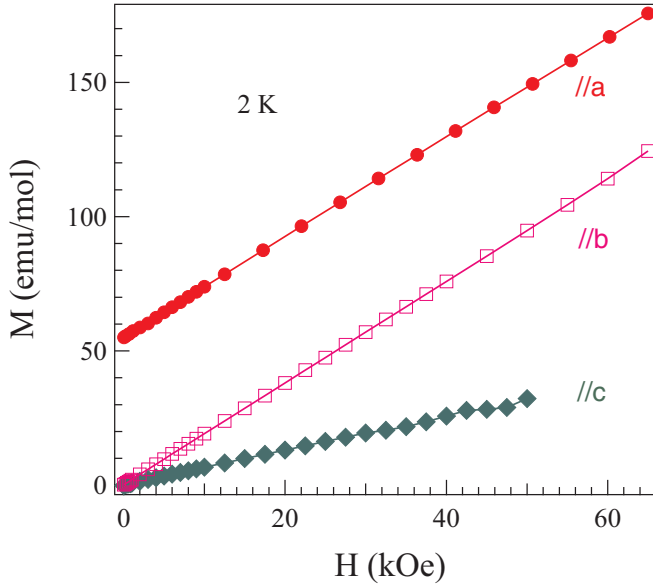
FIG. 3. M(H) curves measured at 2 K along three different crystallographic axes of $Y_{0.7}La_{0.3}VO_3$.

Figure 3 shows the M(H) curves measured at 2 K along three crystallographic axes. A linear field dependence was observed when the external magnetic field is applied along all three crystallographic axes. However, a remanent magnetization of ∼50 emu/mol was observed when the external magnetic field is applied along the *a* axis. This is consistent with the observation of a ferromagnetic component along the *a* axis in Fig. 2.

Thermal conductivity (Fig. 4) of $Y_{0.7}La_{0.3}VO_3$ shows a similar temperature dependence as those of other $Y_{1-x}La_xVO_3$ ($x = 0.40, 0.74, 0.86$, and 1) members [11,26]. A phonon glass behavior above T_N signals strong phonon scattering by spin and orbital fluctuations. The recovery of a regular phonon behavior of thermal conductivity below T_N suggests both spin and orbital ordering across T_N. A slope
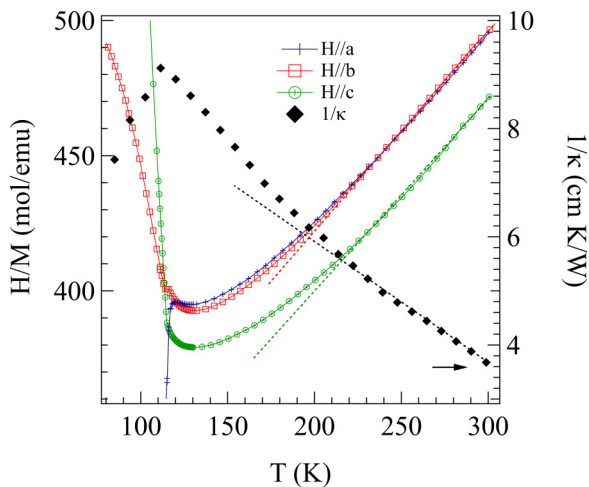

FIG. 4. Temperature dependence of reciprocal magnetization and thermal conductivity of $Y_{0.7}La_{0.3}VO_3$. The dashed lines highlight the slope change around 220 K below which spin-orbital entanglement occurs.
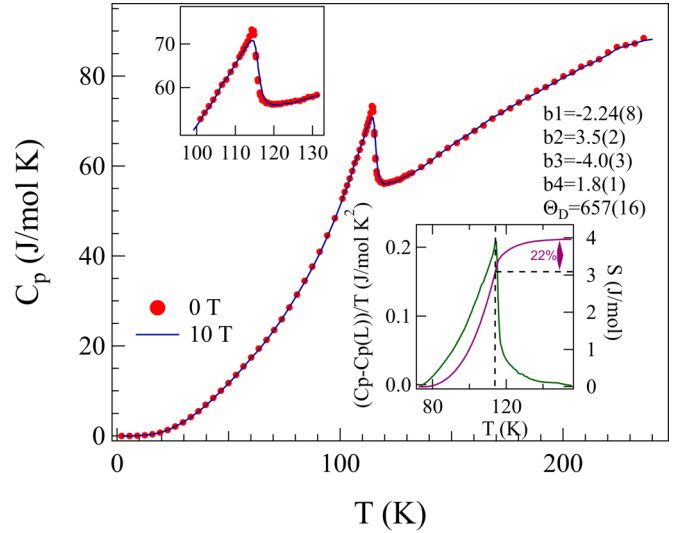

FIG. 5. Temperature dependence of specific heat of $Y_{0.7}La_{0.3}VO_3$ single crystal. The upper inset highlights the details around T_N. The lower inset shows the entropy change across T_N. The parameters estimating the lattice specific heat using the Thirring model are also listed in the figure. b_i ($i = 1$–4) is the fitting parameter in Thirring model [42]: $C_{lattice} = 3NR(1 + b_i\mu^{-n})$, where N is the number of atoms in the unit cell, R is the ideal gas constant, $\mu = (2\pi T/\theta_D)^2 + 1$, and θ_D is the Debye temperature.

change in the temperature dependence of reciprocal thermal conductivity is observed around $T* = 220$ K, where the H/M curves deviate from the linear temperature dependence. This is highlighted in Fig. 4. As reported before [21,26], the slope change signals the transition from orbitally disordered paramagnetic state (labeled disordered state I in Ref. [26]) to the spin-orbital entangled state (labeled disordered state II in Ref. [26]).

Figure 5 shows the temperature dependence of specific heat measured in the magnetic fields of 0 and 100 kOe. Only one lambda-type anomaly was observed around 116 K, where the magnetic order has been determined from the magnetic measurements. This lambda-type anomaly broadens and is shifted slightly to higher temperatures in an external magnetic field of 100 kOe. The entropy release associated with orbital and/or spin ordering across T_N was calculated after subtracting the lattice specific heat estimated using the Thirring model [42]. A total entropy change of 3.76 J/mol K across the transition is similar to that of $Y_{0.50}La_{0.50}VO_3$ and larger than the total entropy change at T_{OO} and T_N for YVO_3 [26,30]. If we define T_N as the temperature where the maximum in the specific-heat curve is located, 22% entropy is released above T_N for $Y_{0.7}La_{0.3}VO_3$, which is less than that in $Y_{0.50}La_{0.50}VO_3$ where the largest variance is expected. The comparison with $Y_{0.50}La_{0.50}VO_3$ and YVO_3 suggests that both orbital and magnetic ordering might take place at $T_N = 116$ K. The lambda-type anomaly suggests that the transition at T_N is of second-order type.

B. Raman spectroscopy

The Raman spectra were measured in both $a(bb)\bar{a}$ and $a(bc)\bar{a}$ polarization configurations in the temperature range
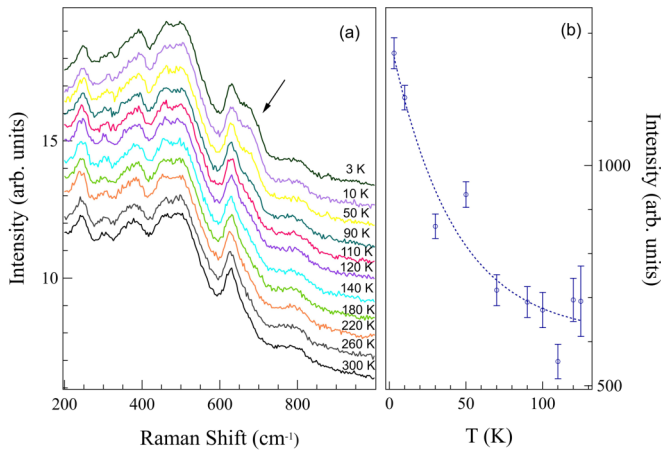
FIG. 6. (a) Raman spectra of $Y_{0.7}La_{0.3}VO_3$ collected in $a(bb)\bar{a}$ configuration at some selected temperatures. The spectra were shifted for clarity. The solid arrow highlights the new band at low temperatures. (b) The intensity of the new band around $680\,cm^{-1}$ below 140 K. The dashed curve is a guide to the eyes. The presence of the band around $680\,cm^{-1}$ signals the C-OO below T_N.

$3\,K \leqslant T \leqslant 300\,K$. Figure 6(a) shows the spectra at some selected temperatures collected in $a(bb)\bar{a}$ configuration. The prominent feature in the spectra is the appearance of a band around $680\,cm^{-1}$ below T_N. As shown in Fig. 6(b), the intensity increases upon cooling. This band is of particular interest and suggests the development of C-OO below T_N [43–46]. This band cannot be resolved in the spectra collected at temperatures above 140 K. As revealed by the synchrotron and neutron diffraction studies presented later, the orthorhombic symmetry is maintained in the whole temperature range. We thus do not expect any new phonon modes, although some energy and intensity changes are likely. The results suggest C-type orbital ordering below T_N and do not suggest the presence of mixed phases below T^*, which are also supported by the Raman spectra collected in the $a(bc)\bar{a}$ polarization configuration.

C. Synchrotron and neutron diffraction

In the G-type orbitally ordered state, RVO$_3$ perovskites have a monoclinic structure ($P2_1/a$) [30]. Compared to the orthorhombic ($Pbnm$) phase of the orbitally disordered state I and the low temperature C-OO/G-AF state, the monoclinic distortion is small and the new reflections forbidden by $Pbnm$ are very weak. The weak reflections cannot be resolved by a conventional laboratory x-ray source or neutron powder diffraction [30]. We thus performed synchrotron single-crystal diffraction measurements in a high resolution mode. The measurements were performed at three temperatures: 298 K in disordered state I, 130 K in disordered state II, and 90 K below T_N. Our careful search did not find any weak reflections, such as (401), violating the $Pbnm$ symmetry. The synchrotron diffraction experiments provide strong evidence for the orthorhombic symmetry for $Y_{0.7}La_{0.3}VO_3$ in all three different temperatures. Thus, the magnetic order below T_N is expected to be G-AF, which is confirmed by neutron-diffraction studies presented below.
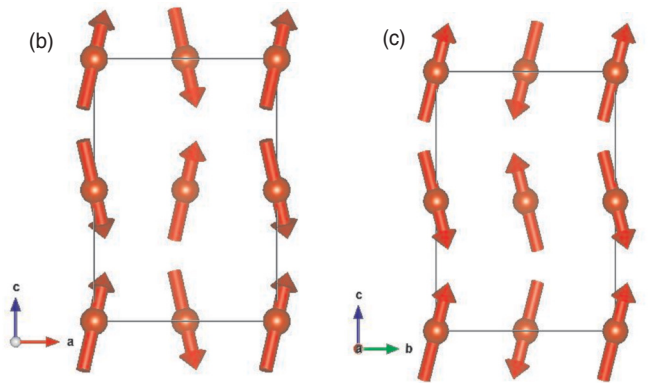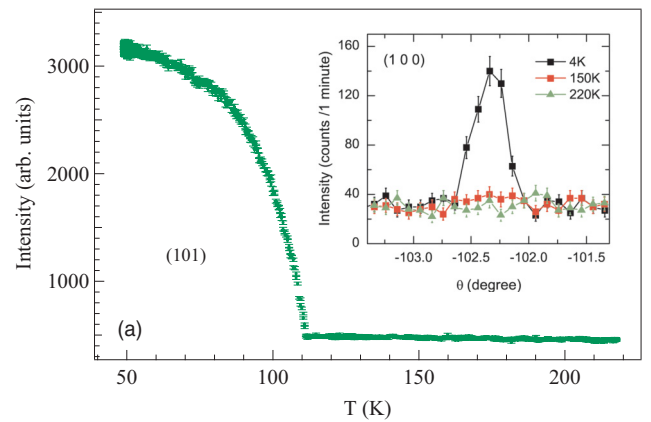

FIG. 7. (a) Temperature dependence of the integrated intensity of (101) reflection in the range $50\,K \leqslant T \leqslant 220\,K$. The inset shows the weak (100) magnetic reflection. (b) The spin alignment in ac plane. (c) The spin alignment in bc plane.

Figure 7(a) shows the temperature dependence of (101) reflection measured on a piece of single crystal at HB1-A, HFIR. This reflection is allowed in $Pbnm$ symmetry and has finite intensity in the paramagnetic states above T_N. Upon cooling across T_N, the intensity increases. The transition temperature determined from this order parameter measurement is 116 K, consistent with that determined from magnetic susceptibility and specific heat measurements. It is interesting to note that (100) reflection is also observed below T_N. The (100) reflection is forbidden to $Pbnm$ and it is absent in synchrotron single crystal diffraction measurement; both point to a magnetic origin of (100) peak. The intensity of this peak is about 1% of (101) reflection and increases below 116 K upon cooling. To further determine the magnetic structure, a neutron single-crystal diffraction study was performed at 5 K using the four-circle diffractometer at the HFIR, ORNL. Representation analyses were performed by BasIreps [47] and SARAh [48]. Four magnetic symmetries $Pbnm$, $Pb'nm'$, $Pb'n'm$, and $Pbn'm'$ are allowed by the structure symmetry $Pbnm$. Only the magnetic symmetry $Pbn'm'$ fits the neutron diffraction data, which is a canted AF structure [see Figs. 7(b) and 7(c)]. The R factor is 0.0378 for 73 reflections at 5 K from the FULLPROF refinement. The refinements are based on combined magnetic and nuclear phases. The moment is $m = [0.32(18)\ 0.38(11)\ 1.40(6)]\mu_B$ with a size of 1.49(8) μ_B. Figures 7(b) and 7(c) show the moment alignment in ac
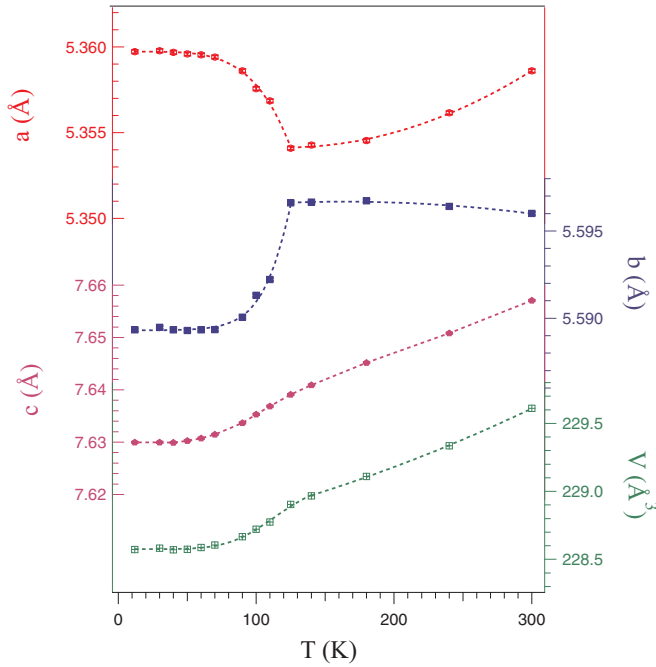
FIG. 8. Temperature dependence of lattice parameters obtained from Rietveld refinement of neutron powder-diffraction patterns.

and *bc* planes, respectively. The canting along the *a* axis is about 14(6)°, which gives a ferromagnetic component along the *a* axis. The canting along the *b* axis is about 12(8)° and the canted moments cancel each other out. The nuclear structure refinements were performed based on 73 and 64 reflections at 5 K and 150 K (the *R* factors are 4.3% and 6.2%), respectively. The V-O bond length and V-O-V bond angle obtained from the refinements agree with the results from neutron powder-diffraction measurements presented later.

We also performed neutron single-crystal diffraction using the WAND located at HFIR and the elastic diffuse scattering spectrometer (Corelli) at SNS to look for possible magnetic or nuclear diffuse scattering in the temperature range $T_N \leqslant T \leqslant T^*$. No sign of any diffuse scattering was observed at 130 K.

Neutron powder diffraction was performed on pulverized single crystals in the temperature range $10\,\mathrm{K} \leqslant T \leqslant 300\,\mathrm{K}$ to study the lattice response to the spin-orbital entanglement and magnetic order. Since no symmetry lowering was observed by synchrotron single-crystal diffraction measurements, all neutron powder diffraction patterns were refined with the orthorhombic symmetry (space group *Pbnm*) using GSAS [49]. Figure 8 shows the temperature dependence of lattice parameters, which shows a clear anomaly across T_N. This temperature dependence agrees with that from powder diffraction using synchrotron [26] and laboratory x-ray results (not shown). The gradual change of *c*-lattice parameter and the unit cell volume across T_N is in contrast to the more abrupt change of *a*- and *b*-lattice parameters. Cooling across T_N, *a* lattice shows an abrupt increase while *b* lattice an abrupt drop. Below 80 K, all lattice parameters show little temperature dependence.

While *c* lattice and the unit cell volume show a nearly linear temperature dependence above T_N, the temperature
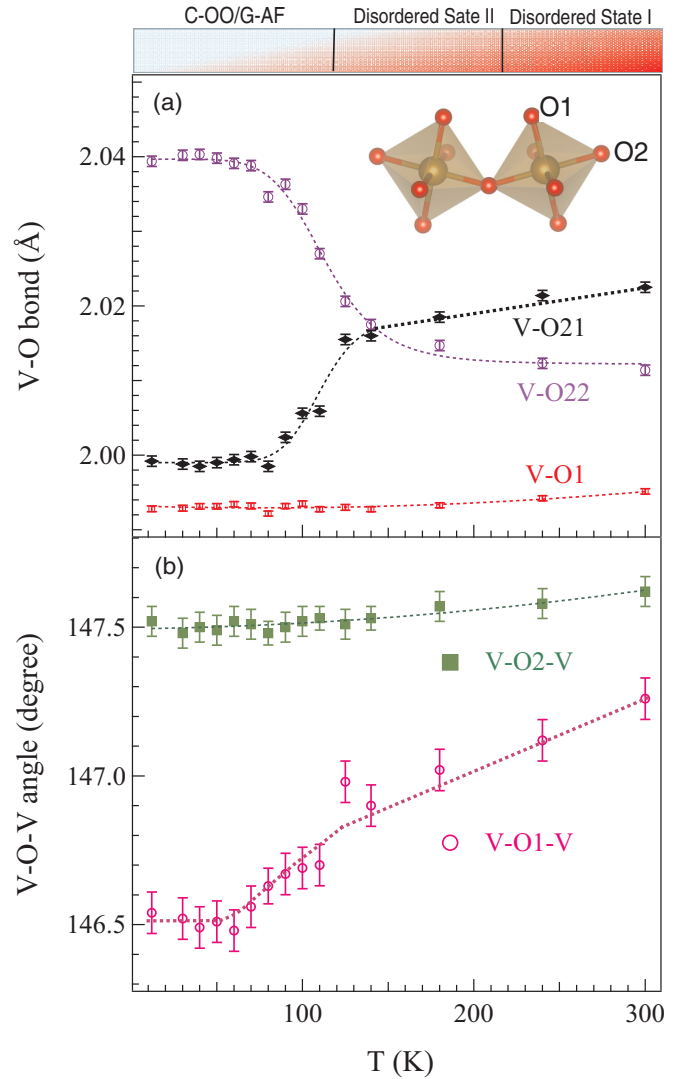

FIG. 9. Temperature dependence of (a) V-O bond lengths and (b) V-O-V bond angles obtained from Rietveld refinement of neutron powder diffraction patterns. The dashed curves are guides for the eye.

dependence of *a*- and *b*-lattice parameters shows a nonlinear temperature dependence. Above T^*, *a* lattice decreases and *b* lattice increases with decreasing temperature. In the temperature range $T_N < T < T^*$, both *a* and *b* lattices show little temperature dependence.

The V-O bond lengths and V-O-V bond angles obtained from the neutron powder diffraction refinements are plotted as a function of temperature and shown in Fig. 9. The out-of-plane V-O1 bond is always the shortest and shows a small temperature dependence in the whole temperature range. This is consistent with the picture that *xy* orbital is always occupied when considering the orbital occupation below room temperature. At room temperature, the V-O1 bond is 1.9951(2) Å, shorter than the two in-plane V-O bonds: V-O21 (along *x* direction) of 2.0114(2) Å and V-O22 (along *y* direction) of 2.0225(2) Å. These bond lengths are comparable to those of YVO3 [30,31]. Upon cooling from room temperature, V-O21 decreases while V-O22 increases and the difference between V-O21 and V-O22 becomes smaller. Cooling across

T_N, V-O21 shows a rapid drop and V-O22 an increase to a saturation value below 80 K. At 12 K, V-O21 (1.9992(2) Å) is comparable to V-O1 (1.9928(2) Å), V-O22 becomes the longest with a bond length of 2.0394(2) Å. This bond length splitting is similar to that in YVO$_3$ below T_{CG} [30,31]

Figure 9(b) shows the temperature dependence of V-O-V bond angles. In the whole temperature range, the in-plane V-O2-V bond angle is larger than the out-of-plane V-O1-V. At room temperature, the V-O-V bond angles $\sim 147°$ are about 3° larger than those of $\sim 144°$ in YVO$_3$ [30,31]. This is consistent with the fact that La^{3+} has a larger ionic radius than Y^{3+} and the partial substitution of Y^{3+} by La^{3+} increases the average ionic radius of the rare-earth site. Above T_N, the in-plane V-O2-V bond angle decreases at a rate of $5.8(8) \times 10^{-4}$ degree per Kelvin with decreasing temperature; below T_N, it shows little temperature dependence. The out-of-plane V-O1-V bond angle decreases while cooling at a much faster rate of $2.2(2) \times 10^{-3}$ degree per Kelvin above T_N; a large drop of ~ 0.3 degree is observed cooling across T_N; below 80 K, V-O1-V bond angle shows little temperature dependence.

IV. DISCUSSION

Our results support a ground state of C-OO and canted G-AF below $T_N = 116$ K for Y$_{0.7}$La$_{0.3}$VO$_3$. The entropy change (Fig. 5) across the magnetic transition is larger than that at T_{OO} or T_N for YVO$_3$. Since only one anomaly was observed at T_N in the temperature dependence of magnetic susceptibility, specific heat, and thermal conductivity, we can conclude that spin and orbital order simultaneously at T_N in Y$_{0.7}$La$_{0.3}$VO$_3$. The synchrotron- and neutron-diffraction studies show that the orthorhombic symmetry is maintained in the whole temperature range investigated in this work. The G-type magnetic ground state and the orthorhombic symmetry rule out G-OO below T_N, which is compatible with C-AF and a monoclinic lattice. The C-OO state below T_N is also supported by the octahedral site distortion and the observed G-type AF order. The V-O bond-lengths below T_N determined by neutron powder diffraction (Fig. 9) are similar to those in YVO$_3$ below 77 K with VO22 > VO21 $\approx$ VO1 [30,31]. The neutron single-crystal diffraction confirmed the G-type AF structure below T_N with the moment direction primarily along c axis. In the orthorhombic $Pbnm$ structure, the Dzyaloshinskii vector $\mathbf{D}_{ij}$ is parallel to the b axis. Thus in the C-OO state below T_N, both the antisymmetric exchange term $\mathbf{D}_{ij} \cdot \mathbf{S}_i \times \mathbf{S}_j$ and a site anisotropy give a ferromagnetic canted-spin component parallel to the a axis. This is confirmed by the magnetic measurements (Figs. 2 and 3).

After confirming the spin and orbital ordering below T_N, we turn to understand disordered state II in the temperature range $T_N < T < T^*$. Is it different from the orbitally disordered paramagnetic state, i.e., disordered state I in Fig. 1? Is it a mixture of orbitally ordered and disordered phases? Or is it a spin-orbital entangled state as proposed in LaVO$_3$ in a similar temperature range? First, the magnetic, electrical, and thermal transport properties distinguish disordered state II from disordered state I. There is a slope change around 220 K in the inverse magnetic susceptibility and inverse thermal conductivity curves. This is highlighted by the dashed line in Fig. 4. This feature is observed in a wide compo-

sition range $0.2 < x \leqslant 1$ as reported in our previous work where we mapped out the spin and orbital ordering phase diagram in Y$_{1-x}$La$_x$VO$_3$ [26]. In LaVO$_3$, the magnitude of thermoelectric power drops dramatically upon cooling through 220 K and approaches zero around 160 K [21]. All these physical properties distinguish disordered state II from disordered state I. Second, our data do not support any mixed-phase scenario in disordered state II. There are four different possible mixed-phase scenarios: (1) C-OO/G-AF with disordered state I, (2) G-OO/C-AF with orbitally disordered state I, (3) G-OO/C-AF and C-OO/G-AF, and (4) G-OO/C-AF, C-OO/G-AF and disordered state I. None of these scenarios is supported by our diffraction studies. The neutron single-crystal diffraction measurement does not show any anomaly in the intensity of (101) and (100) reflections around T^*. This rules out the possible presence of G-AF or C-AF in disordered state II. Our synchrotron and laboratory x-ray diffraction measurements do not see any peak splitting/broadening or any extra reflections. This does not support the presence of G-OO in this temperature range. Our neutron-diffraction measurements using WAND and Corelli, which are two beamlines that are optimized for the observation of elastic diffuse scattering, do not suggest any magnetic or nuclear diffuse scattering. The Raman spectroscopy results shown in Fig. 6 do not suggest the presence of G-OO or C-OO phases in disordered state II. It is worth mentioning that magnetic properties shown in Figs. 2 and 4 suggest short-range magnetic correlations in the temperature range $T_N < T < 130$ K. This is not unexpected and the short-range correlations exist only in a narrow temperature range near T_N. Finally, we would believe the state in the temperature range $T_N < T < T^*$ in Y$_{0.7}$La$_{0.3}$VO$_3$ is the spin-orbital entangled disordered state II as proposed in LaVO$_3$. This is supported by the structural anomaly observed by neutron diffraction in this temperature range.

We first look at the average structure obtained from neutron powder diffraction. The most striking feature of Fig. 9 is that the difference between in-plane V-O21 and V-O22 bonds becomes smaller upon cooling from room temperature and they are comparable in the spin-orbital entangled state. This octahedral site distortion is incompatible with that intrinsic to the $Pbnm$ perovskite compounds and also different from that in the orbitally ordered state. The universal features of lattice distortions in perovskites with orthorhombic $Pbnm$ space group and the biasing effect on orbital ordering in RMO_3 (M = transition metal) have been well addressed by Zhou *et al.* [50–53]. In addition to the GdFeO$_3$-type distortion, which can be described by the tilting system $a^- a^- b^+$ in the Glazer notation, octahedral site distortion leads to, in the ab plane, one long and one short O-M-O bond alternating along the pseudocubic [100] and [010] axes. The difference between the long and short in-plane M-O bonds increases with decreasing temperature since the tolerance factor of perovskites have a positive temperature dependence. At room temperature, the VO$_{6/2}$ octahedra in Y$_{0.7}$La$_{0.3}$VO$_3$ have three inequivalent V-O bonds: V-O21 > V-O22 > V-O1, consistent with the above analysis. However, it is unusual that the difference between V-O21 and V-O22 decreases upon cooling and these two in-plane V-O bonds become comparable in the spin-orbital entangled state. Obviously, the octahedral

site distortion compatible with the spin-orbital entanglement is incompatible with the intrinsic lattice distortion of *Pbnm* perovskites. This incompatibility leads to structural instability responsible for the anomalous thermal conductivity in the spin-orbital entangled state and results in the phase transition from spin-orbital entangled state to the *C*-OO/*G*-AF ground state at $T_N = 116$ K for $Y_{0.7}La_{0.3}VO_3$. In the *C*-OO/*G*-AF state, the bond length relation of V-O22 > V-O21 ≈ V-O1 is similar to that in YVO_3.

The presence of the spin-orbital entanglement in disordered state II is also supported by the local structure distortion revealed by neutron diffraction and the pair distribution function (PDF) analysis. Yano *et al.* [54] investigated the local structure of YVO_3, $Y_{0.9}La_{0.1}VO_3$, and $Y_{0.7}La_{0.3}VO_3$ in the temperature range $5 \leqslant T \leqslant 300$ K. Like in YVO_3, *G*-type orbital order occurs in $Y_{0.9}La_{0.1}VO_3$ in the temperature range $T_{CG} < T < T_{OO}$. The main results of this careful neutron PDF study are (1) For $Y_{0.7}La_{0.3}VO_3$, the experimental data in the whole temperature range can be fitted with a local model that is refined based on the global orthorhombic *Pbnm* structure. A local model based on the global monoclinic $P2_1/a$ structure cannot provide a data fitting of comparable quality. However, the local model based on the average monoclinic $P2_1/a$ structure is needed to simulate the experimental data at $T > T_{CG}$ for YVO_3 and $Y_{0.9}La_{0.1}VO_3$. This local structure suggests that local symmetry does not follow the global one in YVO_3 and $Y_{0.9}La_{0.1}VO_3$ at room temperature. While in $Y_{0.7}La_{0.3}VO_3$ where the *G*-OO is destabilized the La-doping, the local symmetry is the same as the global symmetry. (2) One interesting feature of the local structure obtained from the neutron PDF study is that the difference between the bond lengths of O-O pairs is the smallest in the temperature range $T_N < T < T^*$. At 5 K, the difference between long and short local O-O bonds can be well resolved, suggesting orbital order. The difference becomes smaller at 300 K in disordered state I. However, the difference becomes even smaller in the temperature range $T_N < T < T^*$ and those two O-O pairs are comparable to each other. The evolution with temperature of the local structure is consistent with the average structure discussed above and also supports the presence of spin-orbital entanglement in disordered state II. (3) The partial substitution of Y by La broadens the correlation peaks and suppresses the peak intensity, which indicates significant loss of the coherence of the correlations. This might account for the reduced entropy change across the magnetic order and indicate some fluctuations even below T_N. The loss of the coherence of pair correlations suggests that the rare-earth-site disorder impedes a cooperative Jahn-Teller distortion and favors the spin-orbital entangled state.

Following the classic Jahn-Teller orbital physics, the distinctly different octahedral distortion results in the different orbital occupancy. In both *G*-OO and *C*-OO states, the short in-plane V-O bond is comparable to the out-of-plane V-O1. The orbital occupancy in case of this type of octahedral site distortion is illustrated in Fig. 10(a). The same orbital occupancy is maintained with the trigonal distortion of $VO_{6/2}$ octahedra [55]. Figure 10(b) shows the proposed orbital occupancy with V-O21 ≈ V-O22 > V-O1 as observed in $Y_{0.7}La_{0.3}VO_3$ in the temperature range $T_N \leqslant T \leqslant T^*$. This type of octahedral distortion results in the *yz/zx* orbital de-
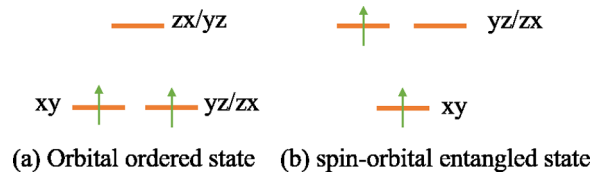

FIG. 10. (a) The orbital occupancy in the orbitally ordered state. (b) the orbital degeneracy in the disordered states I and II.

generacy, which facilitates the spin-orbital entanglement in the temperature range $T_N \leqslant T \leqslant T^*$. It is worth mentioning that *yz/zx* orbitals are also degenerate in disordered state I at $T > T^*$, where the spin and orbital operators can be separated from each other.

The difference between VO21 and VO22 bonds in $Y_{0.7}La_{0.3}VO_3$ around room temperature is much larger than that in $LaVO_3$. If the bond-length difference affects the temperature below which the spin-orbital entanglement occurs, we would expect T^* for $LaVO_3$ is much higher than that for $Y_{0.7}La_{0.3}VO_3$. However, we noticed that T^* is around 200 K and independent of x in $Y_{1-x}La_xVO_3$ ($0.20 < x \leqslant 1$). This signals that T^* does not depend on the difference of the in-plane V-O bonds in $Y_{1-x}La_xVO_3$ or the average $GdFeO_3$ distortion. It is worth mentioning that for RVO_3 members with R = Lu,...,Pr, T_{OO}, where the *G*-type orbital order occurs, is also around 200 K. Similarly, T_{OO} and T^* suggest that the spin-orbital entangled state and *G*-OO state are comparable in energy. This puts some constraint on the theoretical study of the spin-orbital entanglement in RVO_3 perovskites.

The competition between the *G*-OO state and the spin-orbital entangled state in RVO_3 perovskites is biased by the rare-earth-site disorder. $Y_{0.7}La_{0.3}VO_3$ and $EuVO_3$ have similar average ionic radius of the rare-earth site. $EuVO_3$ has a *G*-OO/*C*-AF ground state with $T_{OO} = 204$ K and $T_N = 131$ K [29,56]. The occurrence of spin-orbital entanglement and the *C*-OO/*G*-AF ground state of $Y_{0.7}La_{0.3}VO_3$ highlight the importance of the size variance of the rare-earth site: Rare-earth-site disorder favors the spin-orbital entanglement by impeding the cooperative Jahn-Teller distortion. This is supported by the observation of the spin-orbital entanglement in a wide composition range $0.2 < x < 1$ in $Y_{1-x}La_xVO_3$. The pseudocubic $LaVO_3$ is special where the spin-orbital entanglement wins against *G*-OO without the help of rare-earth-site disorder. For $CeVO_3$, although all studies suggest the *G*-OO/*C*-AF ground state, the sequence of spin and orbital ordering is different. Several groups reported a $T_N = 136$ K, which is followed by a first-order structural transition at $T_t = 131$ K [1,11,38,57]. This sequence of spin and orbital ordering is similar to that in $LaVO_3$. However, Ren *et al.* and Reehuis *et al.* observed an orbital order at $T_{OO} = 154$ K (136 K) and a magnetic order at $T_N = 136$ K(124) [22,58]. The discrepancy signals that the spin and orbital ordering in $CeVO_3$ is sensitive to the stoichiometry which induces disorder and affects the competition between the *G*-OO state and the spin-orbital entangled state.

The spin-orbital entanglement is suppressed in the orbitally ordered state. Considering a weak orbital-lattice coupling for t_{2g} electrons, the quantum fluctuations of the spin-orbital entangled phase might compete with

the G-OO phase below T_{OO} for RVO$_3$ members with $R =$ Lu,...,Pr. Since the orbital flipping transition between G-OO/C-AF and C-OO/G-AF states at T_{CG} only shows up in RVO$_3$ members with $R =$ Lu,...,Dy, it is necessary to take into account the covalency between rare-earth-site cations and oxygens [59] and/or the e-orbital occupation due to a hybridization between t^2 and et configurations [28,53]. The intrasite hybridization, which depends on the trigonal distortion [55], are active for these RVO$_3$ members. The effects of all these factors on the orbital flipping transition at T_{CG} deserve further experimental and theoretical studies.

One important indication of the results presented in this paper is about the nature of transitions at T_N and T_t in LaVO$_3$. LaVO$_3$ shows similar anomalies in the temperature dependence of magnetic susceptibility and thermal conductivity as other Y$_{1-x}$La$_x$VO$_3$ ($0.20 < x < 1$) members. We thus expect similar octahedral site distortions in the spin-orbital entangled state. The magnetic order at T_N for LaVO$_3$ does not result from the magnetic coupling in the paramagnetic state but corresponds to the transition from the spin-orbital entangled state to the C-OO/G-AF state. As in Y$_{0.7}$La$_{0.3}$VO$_3$, the structure is still orthorhombic in the temperature interval $T_t < T < T_N$ for LaVO$_3$. At T_t, C-OO/G-AF is not stable and changes to the G-OO/C-AF, which is the ground state for RVO$_3$ with large rare-earth ions [59]. This orbital flipping transition is a first-order transition and similar to what happens in DyVO$_3$ at low temperatures [53,60,61].

V. SUMMARY

In summary, we investigate the lattice response to the spin-orbital entanglement in Y$_{0.7}$La$_{0.3}$VO$_3$. In the spin-orbital entangled state, the VO$_{6/2}$ octahedra have two comparable in-plane V-O bonds which are longer than the out-of-plane V-O1 bond. This local structural distortion supports the spin-orbital entanglement with degenerate yz/zx orbitals that are partially filled. However, this distortion is incompatible with the octahedral-site distortion intrinsic to the orthorhombic perovskites and their competition induces a second-order transition from the spin-orbital entangled state to the C-OO/G-AF state. The fact that both T^*, below which spin-orbital en-

tanglement occurs in Y$_{1-x}$La$_x$VO$_3$ ($0.20 < x \leqslant 1$), and T_{OO}, below which orbital orders into G-OO in RVO$_3$ ($R =$ Pr,..., Lu, and Y), are around 200 K suggests that these two states are comparable in energy and compete with each other. Their interplay and competition contribute to the rich phase diagrams of spin and orbital ordering in Y$_{1-x}$La$_x$VO$_3$ and RVO$_3$. The rare-earth-site disorder favors the spin-orbital entangled state instead of the cooperative Jahn-Teller distortions. This study indicates a C-OO/G-AF state in the temperature interval $T_t = 141$ K $\leqslant T \leqslant T_N = 143$ K and an orbital flipping transition at T_t for LaVO$_3$.

[1] S. Miyasaka, Y. Okimoto, M. Iwama, and Y. Tokura, Phys. Rev. B **68**, 100406(R) (2003).

[2] J. B. Goodenough, Phys. Rev. **100**, 564 (1955).

[3] J. Kanamori, J. Phys. Chem. Solids **10**, 87 (1959).

[4] G. R. Blake, A. A. Nugroho, M. J. Gutmann, and T. T. M. Palstra, Phys. Rev. B **79**, 045101 (2009).

[5] A. M. Oleś, P. Horsch, and G. Khaliullin, Phys. Rev. B **75**, 184434 (2007).

[6] Y. Motome, H. Seo, Z. Fang, and N. Nagaosa, Phys. Rev. Lett. **90**, 146602 (2003).

[7] M. De Raychaudhury, E. Pavarini, and O. K. Andersen, Phys. Rev. Lett. **99**, 126402 (2007).

[8] G. Khaliullin, P. Horsch, and A. M. Oleś, Phys. Rev. Lett. **86**, 3879 (2001).

[9] Z. Fang and N. Nagaosa, Phys. Rev. Lett. **93**, 176404 (2004).

[10] A. M. Oleś, P. Horsch, L. F. Feiner, and G. Khaliullin, Phys. Rev. Lett. **96**, 147205 (2006).

[11] J.-Q. Yan, J.-S. Zhou, and J. B. Goodenough, Phys. Rev. Lett. **93**, 235901 (2004).

[12] I. V. Solovyev, Phys. Rev. B **74**, 054412 (2006).

[13] J. Reul, A. A. Nugroho, T. T. M. Palstra, and M. Grüninger, Phys. Rev. B **86**, 125128 (2012).

[14] M. Skoulatos, S. Toth, B. Roessli, M. Enderle, K. Habicht, D. Sheptyakov, A. Cervellino, P. G. Freeman, M. Reehuis, A. Stunault, G. J. McIntyre, L. D. Tung, C. Marjerrison, E.

Pomjakushina, P. J. Brown, D. I. Khomskii, C. Rüegg, A. Kreyssig, A. I. Goldman, and J. P. Goff, Phys. Rev. B **91**, 161104(R) (2015).

[15] K. Kugel and D. Khomskii, Sov. Phys. Usp. **25**, 231 (1982).

[16] A. M. Oleś, J. Phys.: Condens. Matter **24**, 313201 (2012).

[17] W. Witczak-Krempa, G. Chen, Y. B. Kim, and L. Balents, Annu. Rev. Condens. Matter Phys. **5**, 57 (2014).

[18] S. Miyasaka, S. Onoda, Y. Okimoto, J. Fujioka, M. Iwama, N. Nagaosa, and Y. Tokura, Phys. Rev. Lett. **94**, 076405 (2005).

[19] Z. Fang, N. Nagaosa, and K. Terakura, Phys. Rev. B **67**, 035101 (2003).

[20] M. Kim, Phys. Rev. B **97**, 155141 (2018).

[21] J.-S. Zhou, Y. Ren, J.-Q. Yan, J. F. Mitchell, and J. B. Goodenough, Phys. Rev. Lett. **100**, 046401 (2008).

[22] Y. Ren, A. A. Nugroho, A. A. Menovsky, J. Strempfer, U. Rütt, F. Iga, T. Takabatake, and C. W. Kimball, Phys. Rev. B **67**, 014107 (2003).

[23] L. D. Tung, A. Ivanov, J. Schefer, M. R. Lees, G. Balakrishnan, and D. McK. Paul, Phys. Rev. B **78**, 054416 (2008).

[24] P. Bordet, C. Chaillout, M. Marezio, Q. Huang, A. Santoro, S. Cheong, H. Takagi, C. Oglesby, and B. Batlogg, J. Solid State Chem. **106**, 253 (1993).

[25] H. Seim, H. Fjellvag, and B. Hauback, Acta Chem. Scand. **52**, 1301 (1998).

[26] J.-Q. Yan, J.-S. Zhou, J. G. Cheng, J. B. Goodenough, Y. Ren, A. Llobet, and R. J. McQueeney, Phys. Rev. B **84**, 214405 (2011).

[27] D. Bizen, K. Nakatsuka, T. Murata, H. Nakao, Y. Murakami, S. Miyasaka, and Y. Tokura, Phys. Rev. B **78**, 224104 (2008).

[28] J.-Q. Yan, J.-S. Zhou, J. B. Goodenough, Y. Ren, J. G. Cheng, S. Chang, J. Zarestky, O. Garlea, A. Llobet, H. D. Zhou, Y. Sui, W. H. Su, and R. J. McQueeney, Phys. Rev. Lett. **99**, 197201 (2007).

[29] R. Fukuta, S. Miyasaka, K. Hemmi, S. Tajima, D. Kawana, K. Ikeuchi, Y. Yamasaki, A. Nakao, H. Nakao, Y. Murakami, and K. Iwasa, Phys. Rev. B **84**, 140409(R) (2011).

[30] G. R. Blake, T. T. M. Palstra, Y. Ren, A. A. Nugroho, and A. A. Menovsky, Phys. Rev. B **65**, 174112 (2002).

[31] M. Reehuis, C. Ulrich, P. Pattison, B. Ouladdiaf, M. C. Rheinstädter, M. Ohl, L. P. Regnault, M. Miyasaka, Y. Tokura, and B. Keimer, Phys. Rev. B **73**, 094440 (2006).

[32] C. Marquina, M. Sikora, M. Ibarra, A. Nugroho, and T. Palstra, J. Magn. Magn. Mater. **290**, 428 (2005).

[33] M. Reehuis, C. Ulrich, K. Prokeš, S. Mat'aš, J. Fujioka, S. Miyasaka, Y. Tokura, and B. Keimer, Phys. Rev. B **83**, 064404 (2011).

[34] M. Martínez-Lope, J. Alonso, M. Retuerto, and M. Fernández-Díaz, Inorg. Chem. **47**, 2634 (2008).

[35] A. Muñoz, J. Alonso, M. Casais, M. Martínez-Lope, J. Martínez, and M. Fernández-Díaz, J. Mater. Chem. **13**, 1234 (2003).

[36] B. C. Chakoumakos, H. Cao, F. Ye, A. D. Stoica, M. Popovici, M. Sundaram, W. Zhou, J. S. Hicks, G. W. Lynn, and R. A. Riedel, J. Appl. Crystallogr. **44**, 655 (2011).

[37] A. V. Mahajan, D. C. Johnston, D. R. Torgeson, and F. Borsa, Phys. Rev. B **46**, 10966 (1992).

[38] H. C. Nguyen and J. B. Goodenough, Phys. Rev. B **52**, 324 (1995).

[39] Y. Ren, T. Palstra, D. Khomskii, E. Pellegrin, A. Nugroho, A. Menovsky, and G. Sawatzky, Nature **396**, 441 (1998).

[40] L. D. Tung, M. R. Lees, G. Balakrishnan, and D. McK. Paul, Phys. Rev. B **75**, 104404 (2007).

[41] A. A. Belik, Inorg. Chem. **52**, 8529 (2013).

[42] H. Thirring, Phys. Z. **14**, 867 (1913).

[43] B. Roberge, S. Jandl, A. A. Nugroho, and T. Palstra, J. Raman Spectroscopy **43**, 127 (2012).

[44] E. Siranidi, D. Lampakis, D. Palles, E. Liarokapis, and T. Palstra, J. Phys.: Conf. Ser. **150**, 042184 (2009).

[45] B. Roberge, M. Balli, S. Jandl, P. Fournier, T. Palstra, and A. Nugroho, J. Phys.: Condens. Matter **28**, 435401 (2016).

[46] S. Miyasaka, J. Fujioka, M. Iwama, Y. Okimoto, and Y. Tokura, Phys. Rev. B **73**, 224436 (2006).

[47] J. Rodríguez-Carvajal, Physica B **192**, 55 (1993).

[48] A. Wills, Physica B **276**, 680 (2000).

[49] B. H. Toby, J. Appl. Crystallogr. **34**, 210 (2001).

[50] J.-S. Zhou and J. B. Goodenough, Phys. Rev. Lett. **94**, 065501 (2005).

[51] J.-S. Zhou and J. B. Goodenough, Phys. Rev. B **77**, 132104 (2008).

[52] J.-S. Zhou, J. A. Alonso, V. Pomjakushin, J. B. Goodenough, Y. Ren, J.-Q. Yan, and J.-G. Cheng, Phys. Rev. B **81**, 214115 (2010).

[53] J.-S. Zhou, J. B. Goodenough, J.-Q. Yan, J.-G. Cheng, K. Matsubayashi, Y. Uwatoko, and Y. Ren, Phys. Rev. B **80**, 224422 (2009).

[54] S. Yano, D. Louca, J. C. Neuefeind, J.-Q. Yan, J.-S. Zhou, and J. B. Goodenough, Phys. Rev. B **90**, 214111 (2014).

[55] S. Landron and M.-B. Lepetit, Phys. Rev. B **77**, 125106 (2008).

[56] L. D. Tung, M. R. Lees, G. Balakrishnan, and D. M. Paul, Phys. Rev. B **76**, 064424 (2007).

[57] A. Muñoz, J. A. Alonso, M. T. Casáis, M. J. Martínez-Lope, J. L. Martínez, and M. T. Fernández-Díaz, Phys. Rev. B **68**, 144429 (2003).

[58] M. Reehuis, C. Ulrich, P. Pattison, M. Miyasaka, Y. Tokura, and B. Keimer, Eur. Phys. J. B **64**, 27 (2008).

[59] T. Mizokawa, D. I. Khomskii, and G. A. Sawatzky, Phys. Rev. B **60**, 7309 (1999).

[60] S. Miyasaka, T. Yasue, J. Fujioka, Y. Yamasaki, Y. Okimoto, R. Kumai, T. Arima, and Y. Tokura, Phys. Rev. Lett. **99**, 217201 (2007).

[61] J.-Q. Yan, H. B. Cao, M. A. McGuire, Y. Ren, B. C. Sales, and D. G. Mandrus, Phys. Rev. B **87**, 224404 (2013).